

Radiation, clouds, and self-aggregation in RCEMIP simulations

Article

Published Version

Creative Commons: Attribution 4.0 (CC-BY)

open access

Pope, K. N., Holloway, C. E. ORCID: <https://orcid.org/0000-0001-9903-8989>, Jones, T. R. ORCID: <https://orcid.org/0000-0002-7669-1499> and Stein, T. H. M. ORCID: <https://orcid.org/0000-0002-9215-5397> (2023) Radiation, clouds, and self-aggregation in RCEMIP simulations. *Journal of Advances in Modeling Earth Systems*, 15 (2). e2022MS003317. ISSN 1942-2466 doi: 10.1029/2022MS003317 Available at <https://centaur.reading.ac.uk/110661/>

It is advisable to refer to the publisher's version if you intend to cite from the work. See [Guidance on citing](#).

To link to this article DOI: <http://dx.doi.org/10.1029/2022MS003317>

Publisher: American Geophysical Union

All outputs in CentAUR are protected by Intellectual Property Rights law, including copyright law. Copyright and IPR is retained by the creators or other copyright holders. Terms and conditions for use of this material are defined in the [End User Agreement](#).

www.reading.ac.uk/centaur

CentAUR

Central Archive at the University of Reading

Reading's research outputs online



RESEARCH ARTICLE

10.1029/2022MS003317

Special Section:

Using radiative-convective equilibrium to understand convective organization, clouds, and tropical climate

Key Points:

- General Circulation Models (GCMs) aggregate faster than Cloud-system Resolving Models (CRMs) on average due to an enhanced longwave feedback
- Feedbacks tend to decrease in magnitude as sea surface temperature increases, although the rate of aggregation remains similar
- Aggregation rate in GCMs is correlated with diabatic feedbacks, while in CRMs it is more related to advection feedbacks

Correspondence to:

K. N. Pope,
k.n.pope@pgr.reading.ac.uk





Citation:

Pope, K. N., Holloway, C. E., Jones, T. R., & Stein, T. H. M. (2023). Radiation, clouds, and self-aggregation in RCEMIP simulations. *Journal of Advances in Modeling Earth Systems*, 15, e2022MS003317. <https://doi.org/10.1029/2022MS003317>

Received 21 JUL 2022

Accepted 9 FEB 2023

Radiation, Clouds, and Self-Aggregation in RCEMIP Simulations

K. N. Pope¹ , C. E. Holloway¹ , T. R. Jones¹ , and T. H. M. Stein¹ 

¹Department of Meteorology, University of Reading, Reading, UK

Abstract The responses of tropical anvil cloud and low-level cloud to a warming climate are among the largest sources of uncertainty in our estimates of climate sensitivity. However, most research on cloud feedbacks relies on either global climate models with parameterized convection, which do not explicitly represent small-scale convective processes, or small-domain models, which cannot directly simulate large-scale circulations. We investigate how self-aggregation, the spontaneous clumping of convection in idealized numerical models, depends on cloud-radiative interactions with different cloud types, sea surface temperatures (SSTs), and stages of aggregation in simulations that form part of RCEMIP (the Radiative-Convective Equilibrium Model Intercomparison Project). Analysis shows that the presence of anvil cloud, which tends to enhance aggregation when collocated with anomalously moist environments, is reduced in nearly all models when SSTs are increased, leading to a corresponding reduction in the aggregating influence of cloud-longwave interactions. We also find that cloud-longwave radiation interactions are stronger in the majority of General Circulation Models (GCMs), typically resulting in faster aggregation compared to Cloud-system Resolving Models (CRMs). GCMs that have stronger cloud-longwave interactions tend to aggregate faster, whereas the influence of circulations is the main factor affecting the aggregation rate in CRMs.

Plain Language Summary The spatial organization of tropical rainstorms has major effects on weather and climate. This organization influences the duration and intensity of these convective storms, and alters the amount of radiation absorbed and emitted by the atmosphere. There is great uncertainty in the response of organization to a warming climate, and this results in one of the largest sources of uncertainty in climate predictions. Climate projections rely on either General Circulation Models (GCMs) that can represent the large-scale motions, or smaller high-resolution models that represent small-scale features like cloud formations, but not the large motions. In this study, we compare convective organization in GCMs and Cloud-system Resolving Models (CRMs) across a range of sea surface temperatures (SSTs). We find that the cloud-radiation feedbacks that make the convective environment more favorable for further convection, and the non-convective environment less favorable for convection, are stronger in GCMs than CRMs on average. This is related to larger cloud amounts in GCMs, leading GCMs to have typically faster organization than CRMs. We find these feedbacks which drive aggregation decrease as SST increases, yet the aggregation rate is largely insensitive to SST because of the decrease in the effect of atmospheric motions that oppose aggregation.

1. Introduction

Convective self-aggregation is the process by which initially randomly distributed convection becomes spontaneously clustered despite homogeneous boundary conditions and forcing. It was first identified in numerical models of radiative-convective equilibrium (RCE) (Held et al., 1993), and has major implications for weather and climate (e.g., Wing et al., 2017). Because of this, it has been the focus of many studies in recent years (e.g., Bretherton et al., 2005; Coppin & Bony, 2015) and continues to be an active area of research. Processes that drive and maintain self-aggregation have been shown to be relevant to observed convection (Holloway et al., 2017), aiding the development of tropical cyclones (Nolan et al., 2007) and the Madden-Julian oscillation (Arnold & Randall, 2015; Raymond & Fuchs, 2009). However, there remains much debate as to the mechanisms and feedbacks responsible for controlling aggregation, which is in part due to the inter-model variability in the structures and dynamics of convection within these models (Wing et al., 2017).

Aggregation of tropical convection has significant impacts on the climate, tending to decrease the total high-cloud fraction and free-troposphere humidity (e.g., Bony et al., 2020; Tobin et al., 2013; Wing & Cronin, 2016), affecting the amount of shortwave radiation being absorbed by the atmosphere and surface, as well as affecting the

amount of longwave radiation escaping to space. The uncertainty in the response of aggregation to a warming climate is a major source of uncertainty in our estimates for the global climate sensitivity (Sherwood et al., 2020), with models that increase in aggregation with warming tending to have a lower climate feedback parameter due to increased longwave cooling (Becker & Wing, 2020).

Various metrics have been proposed to characterize aggregation, many of which divide the domain into regions where convection occurs and regions of subsidence. Wing and Emanuel (2014) designed a framework to study aggregation using a variance of frozen moist static energy (FMSE) budget. FMSE, or h , is given by

$$h = c_p T + gz + L_v q_v - L_f q_i \quad (1)$$

where c_p is the specific heat capacity of dry air at constant pressure, T is temperature, g is the gravitational acceleration, z is the height above the surface, L_v is the latent heat of vapourization, q_v is the water vapor mixing ratio, L_f is the latent heat of fusion and q_i is the condensed ice mixing ratio. As aggregation increases, the spatial variance of column-integrated FMSE increases. In RCE experiments over a fixed sea surface temperature (SST), variations in humidity contribute the most to the spatial variability in FMSE as horizontal temperature gradients are weak, and the gravitational potential term is approximately uniform throughout the domain. Therefore the variance of column-integrated FMSE correlates most strongly with the variance of column relative humidity. Wing and Emanuel (2014) derive a budget equation for the rate of change of vertically-integrated FMSE variance, allowing for the quantification of the contributions of different FMSE feedbacks to the rate of change of aggregation:

$$\frac{1}{2} \frac{\partial \hat{h}^2}{\partial t} = \hat{h}' LW' + \hat{h}' SW' + \hat{h}' SEF' - \hat{h}' \nabla_h \cdot \mathbf{u} \hat{h} \quad (2)$$

where hats (^) denote a density-weighted vertical integral, LW and SW are the net atmospheric column longwave and shortwave heating rates, SEF is the surface enthalpy flux, made up of the surface latent heat and sensible heat fluxes, $\nabla_h \cdot \mathbf{u} \hat{h}$ is the horizontal divergence of the \hat{h} flux, and primes (') indicate local anomalies from the instantaneous domain-mean. The net column longwave and shortwave radiative heating rates are defined as the column radiative flux convergence as follows:

$$LW = LW \uparrow_{\text{sfc}} - LW \downarrow_{\text{sfc}} - LW \uparrow_{\text{top}} \quad (3)$$

$$SW = SW \downarrow_{\text{top}} - SW \uparrow_{\text{top}} - SW \downarrow_{\text{sfc}} + SW \uparrow_{\text{sfc}} \quad (4)$$

where upward and downward arrows indicate upwelling and downwelling fluxes, and the subscripts (_{sfc}) and (_{top}) indicate a radiative flux at the surface and at the top of the atmosphere, respectively. Each term on the right hand side of Equation 2 is a covariance between the \hat{h} anomaly and the anomaly of a source/sink of \hat{h} . If the term is positive, there is either an anomalous source of \hat{h} in a region of already high \hat{h} , or an anomalous sink of \hat{h} in a region of low \hat{h} , representing a positive feedback on self-aggregation. Wing and Emanuel (2014) find each of the terms are important for aggregation, with the longwave and surface flux feedback being crucial drivers of aggregation, but later decreasing and becoming negative as the convection becomes aggregated. They find the shortwave feedback to be a key maintainer of aggregation highlighting that the processes that drive aggregation are separate to the processes that maintain it.

Most research on cloud feedbacks relies on either general circulation models (GCMs) that use parameterized convection, or limited-area cloud-system resolving models (CRMs) with explicit convection that are too small to represent global-scale circulations. The climate feedback and sensitivity of aggregation are different for GCMs and CRMs in the Radiative-Convective Equilibrium Model Intercomparison Project (RCEMIP; Wing et al., 2018, 2020), with GCMs typically having a lower climate sensitivity due to convection becoming more aggregated on average at higher SSTs (Becker & Wing, 2020). This response is not seen on average in CRMs.

Despite there being debate as to the processes driving and maintaining aggregation, the majority of studies find that interactions between convection, clouds, and longwave radiation are key drivers and maintainers of aggregation (Wing et al., 2017). Pope et al. (2021) quantified the contribution of direct radiative interactions with different cloud types to longwave and shortwave feedbacks with FMSE using a set of simulations from the UK Met Office Unified Model which are submitted to RCEMIP as UKMOi-vn11.0-RA1-T (referred as UKMO-RA1-T hereafter). They used a similar FMSE variance budget framework to Wing and Emanuel (2014) but normalize \hat{h}

in such a way so that its SST dependence is eliminated, thus making the analysis framework insensitive to SST. They found the direct longwave interactions with high-topped cloud and clear regions to be the main drivers of aggregation. High-topped clouds typically occur in anomalously-high \hat{h} regions and drastically decrease atmospheric radiative cooling, leading to a positive longwave-FMSE feedback. Similarly, clear regions have anomalously high radiative cooling rates and tend to be found in anomalously-low \hat{h} regions, again leading to a positive longwave-FMSE feedback and driving aggregation.

Pope et al. (2021) found the main maintainers of aggregation were longwave interactions with high-topped cloud, and shortwave interactions with water vapor. The shortwave-water vapor feedback contributes 87%–96% of the total shortwave feedback during the mature phase of aggregation, with cloud-shortwave interactions being less important at higher SSTs and higher degrees of aggregation. Anomalously humid environments occur in positive \hat{h}' regions and are able to absorb more solar radiation leading to a positive feedback. The difference in humidity between the moist and dry regions increases with aggregation, hence the shortwave-moisture feedback has a higher impact during mature aggregation. The extents of the contributions of these feedbacks to aggregation are sensitive to SST. In their simulations, the longwave contribution to aggregation is insensitive to SST during the growth phase of aggregation, but there is a smaller longwave contribution to aggregation maintenance as SST increases due to the reduction of high-topped cloud fraction. This decrease in high-topped cloud fraction is consistent with the stability iris mechanism described by Bony et al. (2016), who describe the reduction in anvil cloud as a consequence of increased anvil stability and decreased convective outflow with increasing SST. Shortwave interactions with moisture become less important to aggregation maintenance at warmer SSTs. This is because the variability in atmospheric solar heating between humid and dry regions contributes to a smaller fraction of the total \hat{h} variability as SST increases. Despite radiative interactions with cloud and moisture being the main drivers of aggregation, the rate of aggregation was most strongly moderated by circulations that generally oppose aggregation, resulting in faster aggregation at warmer SSTs.

Wing et al. (2020) showed that the UKMO-RA1-T model is an outlier compared to the other RCEMIP models in several ways. With the upper troposphere being almost fully saturated, it has one of the largest high cloud fractions and one of the smallest low cloud fractions compared to the other models. In addition, out of all the small 100×100 km domain simulations, the UKMO-RA1-T simulations are the only ones that display aggregation. This highlights that the conclusions from Pope et al. (2021) are only strictly applicable to the simulations they studied and may not, in some cases, be relevant for other simulations and real-world convection.

In this study, we test the robustness of the conclusions from Pope et al. (2021) by applying their analysis framework to the CRM and GCM simulations in RCEMIP. We quantify the contributions of cloud-radiation interactions to self-aggregation at different stages of organization and study their SST dependence. We investigate whether the differences in cloud-radiation interactions between models and model types can explain the differences in the behavior of self-aggregation.

2. Methods

The CRMs and GCMs of RCEMIP are configured using a strict protocol which is described in Wing et al. (2018). CRMs perform ~ 100 -day, non-rotating, long channel simulations on a domain of $\sim 6,000 \times 400$ km with a 3 km horizontal grid spacing, doubly periodic boundary conditions, and explicit convection. GCMs perform $\sim 1,000$ -day, non-rotating, global-scale aquaplanet simulations with parameterized convection. They have a mean grid spacing of $\mathcal{O}(1^\circ)$ varying between ~ 100 km and ~ 170 km, with the average of all GCMs being ~ 120 km. Every model in RCEMIP has constant solar forcing and performs simulations with three fixed SSTs of 295 K, 300 and 305 K to compare how convection in RCE may be affected by a warming climate.

We study aggregation using the variance of normalized FMSE budget framework that is described by Pope et al. (2021) (referenced as P21 hereafter). The framework is based on that used in Wing and Emanuel (2014), however vertically-integrated FMSE is normalized between hypothetical upper and lower limits based on SST in an attempt to eliminate the strong temperature dependence of FMSE. This approach uses the variance of normalized FMSE ($\text{var}(\hat{h}_n)$) as the aggregation metric because it is approximately insensitive to SST. The budget equation for the rate of change of $\text{var}(\hat{h}_n)$ is:

$$\frac{1}{2} \frac{\partial \hat{h}_n^2}{\partial t} = \hat{h}_n' LW_n' + \hat{h}_n' SW_n' + \hat{h}_n' SEF_n' - \hat{h}_n' \nabla_h \cdot \mathbf{u} \hat{h}_n \quad (5)$$

Here, \hat{h}'_n and each of the three normalized flux anomalies on the RHS (LW'_n , SW'_n , and SEF'_n) is equal to the original flux anomaly in Equation 2 divided by the difference between the upper and lower limits of \hat{h} (\hat{h}_{\max} and \hat{h}_{\min}). \hat{h}_{\max} is defined as the vertically-integrated FMSE of a fully saturated moist pseudoadiabatic profile from the surface to the tropopause, plus the integrated FMSE of the initial profile above the tropopause. For \hat{h}_{\min} , the vertically-integrated FMSE of a dry adiabatic profile with zero moisture is used within the troposphere, and integrated FMSE above the tropopause from the initial profile is added. The SST is used as the temperature at sea-level pressure to initiate both adiabatic profiles. The tropopause is defined as the lowest level in the initial profile at which the lapse rate decreases to 2°C/km or less, which has some variability in height between model simulations.

To make the comparison between CRMs and the 40× coarser GCMs as fair as possible, we horizontally smooth the raw output fields of the CRMs so that every grid box is the mean of the 40 × 40 grid boxes surrounding it (accounting for the periodic boundary conditions). This is because $\text{var}(\hat{h}_n)$ is not only dependent on spatial aggregation, but it is also sensitive to grid spacing, particularly while convection is well-scattered (analysis not shown). This is due to small-scale features, for example, convective updrafts and downdrafts that tend to have strong positive and negative \hat{h}'_n respectively, not being resolved at coarser resolutions. This leads to a smaller $\text{var}(\hat{h}_n)$ for coarser horizontal resolutions. As the size of the convective clusters increase and \hat{h}_n anomalies are strong over large areas, $\text{var}(\hat{h}_n)$ becomes relatively less sensitive to grid spacing. For example, when the CRMs have a $\text{var}(\hat{h}_n)$ of 1×10^{-4} , the average $\text{var}(\hat{h}_n)$ after smoothing is around 60% lower. When $\text{var}(\hat{h}_n)$ is 1×10^{-3} for CRMs, the $\text{var}(\hat{h}_n)$ after smoothing is around 25% lower. When using this smoothing technique in the analysis, we refer to the CRMs as Smoothed CRMs. Assuming that GCMs represent their subgrid scale processes in a similar way to how CRMs resolve them, we would expect similar results between GCMs and Smoothed CRMs.

In a similar way to P21, we define Growth and Mature phases of aggregation by two ranges of $\text{var}(\hat{h}_n)$ for which convection is randomly scattered or strongly clustered, respectively. The $\text{var}(\hat{h}_n)$ ranges used in this study vary slightly from P21. This is so that as many simulations as possible have a defined Growth and Mature period which satisfy the aforementioned criteria, while the $\text{var}(\hat{h}_n)$ ranges remain small. Note that not all models reach the Mature phase because these models do not appear strongly clustered at any point in time. The Growth phase is identified as any time after day 2 (to neglect spin-up effects) when $\text{var}(\hat{h}_n)$ for GCMs and Smoothed CRMs is between 0.8×10^{-4} and 2.4×10^{-4} . The Mature phase is identified as any time when $\text{var}(\hat{h}_n)$ for GCMs and Smoothed CRMs is between 0.8×10^{-3} and 2.4×10^{-3} . Further justification of these ranges is given in Section 3.1. Given our previous notion that $\text{var}(\hat{h}_n)$ is sensitive to grid spacing, we use the times of the Growth and Mature phases identified from the Smoothed CRMs to also analyze the (non-Smoothed) CRMs.

Since \hat{h}'_n is a factor of every term in Equation 5, one might expect the magnitude of the terms to increase with aggregation. By dividing each term by the instantaneous horizontal standard deviation of \hat{h}_n , we can eliminate the dependence of the terms on the magnitude of \hat{h}'_n . After dividing by this standard deviation, the sensitivity of the terms to aggregation will depend on the sensitivity of the other variable in the term and its correlation with \hat{h}'_n .

A drawback of the $\text{var}(\hat{h}_n)$ budget framework is that it is a vertically-integrated framework that is not able to quantify the effects of processes occurring at specific vertical levels. Studies have shown that there are many low-level processes that are important for aggregation. For example, Muller and Held (2012) highlight the importance of shallow, radiatively-driven circulations caused by cooling atop shallow clouds in dry regions, yielding an upgradient transport of FMSE, inducing a positive aggregation feedback. Jeevanjee and Romps (2013) describe how cold pools are responsible for the domain size dependence of self-aggregation. Boundary layer processes are key for the production of available potential energy that is associated with the development of self-aggregation (Yang, 2018a), and are theorized to determine the length scale of aggregation (Yang, 2018b). Chen and Wu (2019) show that low-level FMSE transport is crucial for the development of aggregation within interactive SST simulations. The use of our vertically-integrated framework means the effects of these processes are not directly studied. Circulations that are induced by diabatic forcing are included in the vertically-integrated

Table 1
Outgoing Shortwave Radiation and Outgoing Longwave Radiation
Thresholds Used to Define the Cloud Types

| Cloud type | OSR (W m^{-2}) | OLR (W m^{-2}) |
|------------|---------------------------|---------------------------|
| Clear | <100 | N/A |
| Shallow | ≥ 100 | >250 |
| Other | ≥ 100 | 173–250 |
| Deep | ≥ 100 | <173 |

advection term in the $\text{var}(\hat{h}_n)$ budget framework. So the radiation and surface enthalpy flux terms only account for the *direct* diabatic feedbacks.

2.1. Cloud Classification Scheme

We use a cloud classification scheme to define a cloud type at each grid point in the simulations. The contribution of radiative interactions with these cloud types to aggregation are calculated by multiplying each cloud type's fraction by the mean covariance between its radiative and FMSE anomalies. This analysis technique is based on that used by P21, however the cloud type definitions in this study are different. In RCEMIP, 3D data are only available

for the final 25 days of CRMs and GCMs, so we are not able to define cloud based on the vertical profile of condensed water for the full simulation as in P21. Instead, we define clouds using top of atmosphere (TOA) fluxes, using the same method as Becker and Wing (2020) (referenced as BW20 hereafter). This method produces four different cloud types: Clear, Shallow, Deep, and Other. The outgoing shortwave radiation (OSR) and outgoing longwave radiation (OLR) thresholds used to define the four cloud types are shown in Table 1. Note that the thresholds in Table 1 are used for each SST. Also note the convention of capitalizing these cloud categories. The Clear category is not to be confused with clear-sky radiation - the radiative fluxes calculated by excluding any cloud from a particular scene.

A comparison of the cloud type classification schemes between that used in P21 and this study is shown in Figures 1a–1d. These figures show the P21 cloud distributions for each of the BW20 cloud types across all of the CRMs. This comparison uses data from the final 25 days of the simulations; the period for which 3D data is

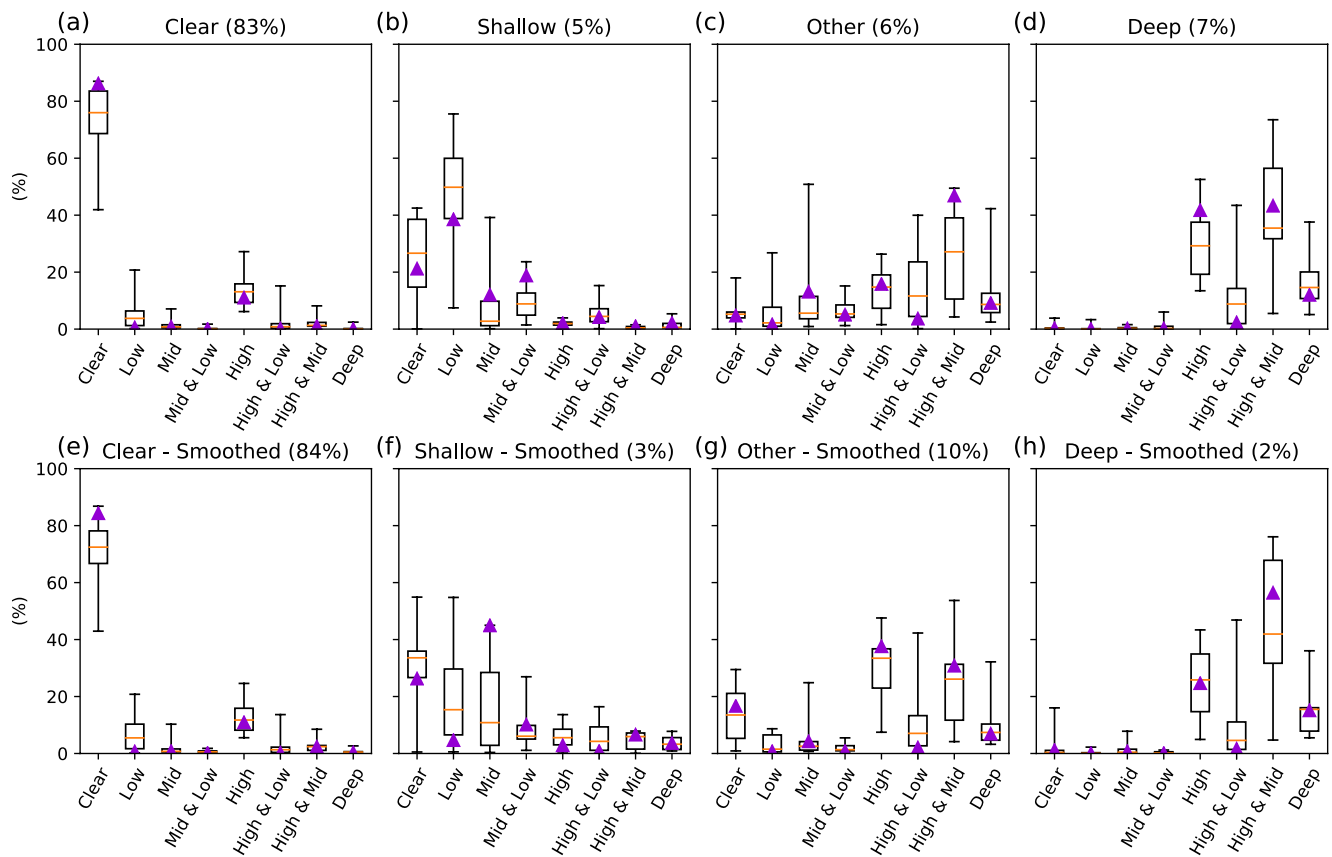


Figure 1. (a–d) Distributions of the cloud categories used in P21 for each of the four cloud types used in this study. (e–h) Distributions of the cloud categories used in P21 for each of the Smoothed cloud types. Data is averaged over the final 25 days of the Cloud-system Resolving Models for all sea surface temperatures. Orange lines represent the median, boxes represent the interquartile range, and whiskers represent the full range of the models. The UKMO-RA1-T model is shown in purple triangles. Average domain fraction is shown in the subplot titles.

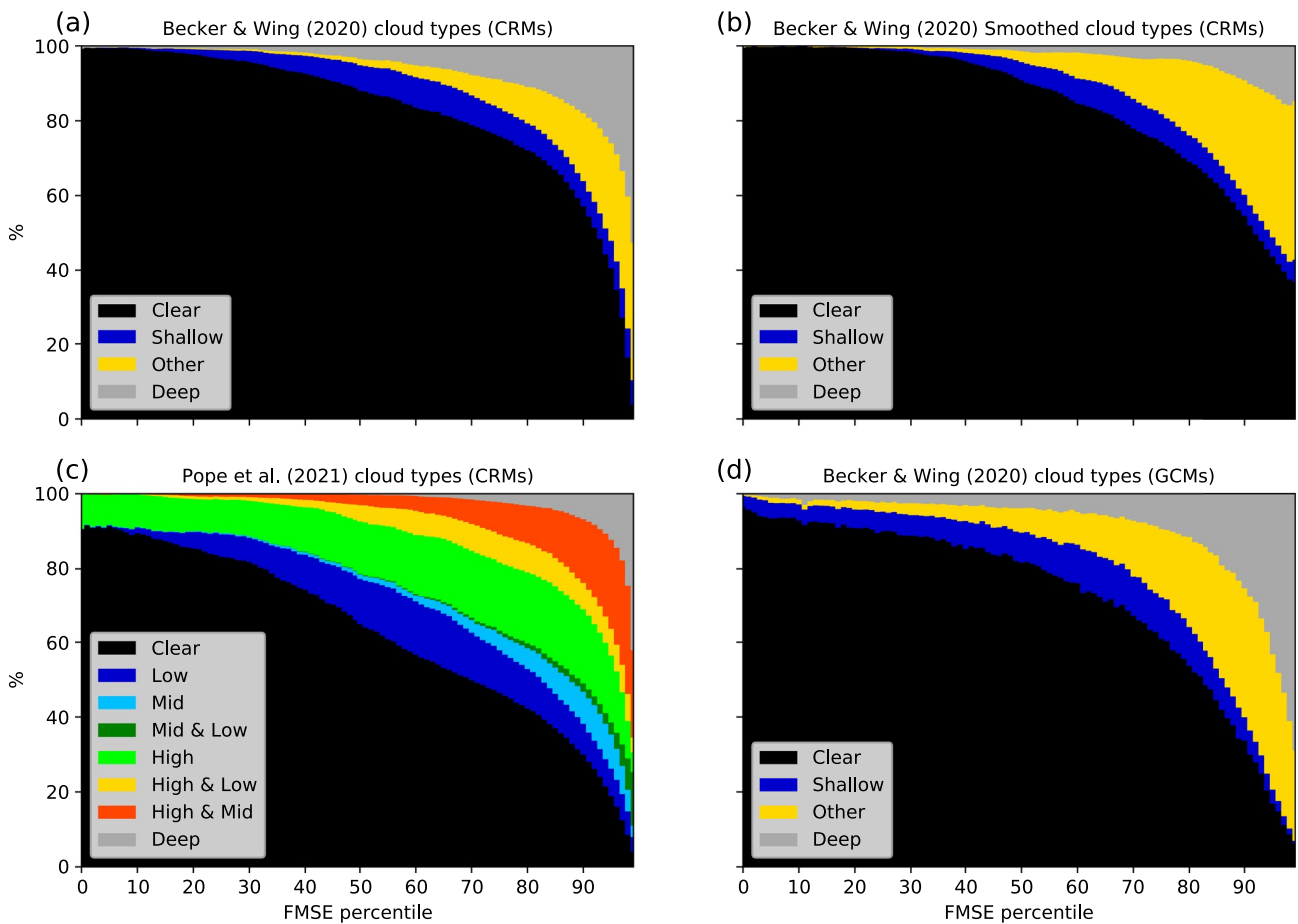


Figure 2. Cloud type fraction versus frozen moist static energy percentile for the (a) BW20 cloud types for all Cloud-system Resolving Models (CRMs), (b) Smoothed BW20 cloud types for all CRMs, (c) P21 cloud types for all CRMs, and (d) BW20 cloud types for the General Circulation Models during the final 24 hr of the simulations.

available. Approximately 80% of this study's Clear category is made up of the Clear type defined in P21, meaning the condensed water content is less than $10^{-6} \text{ kg m}^{-3}$ everywhere in the column. The remainder of the BW20 Clear category is mostly made up of optically-thin High and Low cloud. The Shallow cloud type is mostly made up of Low cloud, and the Deep cloud is almost entirely made up of the high-topped cloud (High, High & Mid, High & Low, and Deep). The Other cloud type is made up of approximately two thirds high-topped cloud that is perhaps too optically thin or having too small a vertical extent to lead to an OLR less than 173 W m^{-2} and be classed as Deep.

Cloud types are redefined using the Smoothed radiative fluxes in order to make a fairer comparison to GCMs. The distribution of the P21 cloud types for each Smoothed cloud type is shown in Figures 1e–1h. Again, this comparison uses data for the final 25 days of the simulations. The Smoothed Clear and Deep categories are mainly made up of the P21 Clear and high-topped cloud categories respectively. There is little difference between the Smoothed and non-Smoothed distributions for these cloud types. The Smoothed Shallow cloud is mostly made up of Clear and low to mid-topped cloud. The Smoothed Other cloud type is mostly composed of high-topped cloud. The main difference between the non-Smoothed and Smoothed distributions is the increase in fraction of Smoothed Other cloud and the decrease in fraction of the Smoothed Deep cloud.

Figure 2 shows the fraction of different cloud types as a function of FMSE percentile during the final 24 hr of the simulations. Differences in the BW20 and P21 cloud classification schemes within the CRMs can be seen by comparing Figures 2a and 2c. Cloud fraction increases with FMSE percentile regardless of the cloud classification scheme used. There is a lower cloud fraction in the BW20 cloud types compared to the P21 cloud types at all FMSE percentiles except for the extremely moist environments in which the cloud fraction is close to 100%.

There is greater high-topped cloud in the P21 classification scheme compared to the BW20 Deep cloud which may be due to the presence of optically-thin High cloud that has $OSR < 100 \text{ W m}^{-2}$. There is also a greater fraction of P21 Low cloud compared to BW20 Shallow cloud at all FMSE percentiles, again due to the presence of optically thin Low cloud with $OSR < 100 \text{ W m}^{-2}$.

The effect of Smoothing is shown by comparing Figure 2a with Figure 2b. Smoothing reduces the total cloud fraction in the lower 40% and upper 10% of FMSE values. The fraction of Deep cloud is reduced and the fraction of Other cloud is increased at all FMSE percentiles. The difference between Smoothed CRMs and GCMs can be seen by comparing Figures 2b and 2d. There is a greater cloud fraction in GCMs at all FMSE percentiles, which is largely due to the increase in Deep cloud fraction. There is also a greater Shallow cloud fraction particularly at lower FMSE values, and a lower Other cloud fraction at higher FMSE values. The effects of Smoothing, and comparisons between CRMs and GCMs are discussed further in Section 4. The cloud type fractions of the non-Smoothed CRMs are most similar to the fractions of the GCMs, suggesting GCMs may be tuned to have a more accurate cloud fraction in a discrete grid box sense rather than on subgrid scales. Yet GCMs still have a greater average cloud fraction particularly at higher \hat{h}_n regions.

Radiative interactions with high-topped cloud and Clear regions are shown to have the largest role in aggregation in P21. With the majority of BW20 Clear and Deep clouds being collocated with P21 Clear and high-topped cloud respectively, results from P21 can be fairly compared to results from this study.

3. Variance of Normalized FMSE

3.1. Evolution of Normalized FMSE Variance in RCEMIP Simulations

The RCEMIP CRMs simulate a wide range of convective characteristics (animations of normalized FMSE anomaly for all models can be found on Zenodo, which is linked to in the Open Research section). All models analyzed in this study display aggregation to some degree except for the UKMO-CASIM model at 305 K, whose convection remains scattered throughout the entire simulation. Figure 3 shows 24-hr running averages of $\text{var}(\hat{h}_n)$ for each Smoothed CRM and SST. Also shown are the $\text{var}(\hat{h}_n)$ limits for the Growth and Mature phase of aggregation (introduced in Section 2) which will be discussed in Sections 3.2 and 4. There is much variability in the rate of aggregation amongst the CRMs as well as the maximum degree of aggregation, with no consistent SST dependence. The inconsistent SST dependence of aggregation is seen regardless of aggregation metric used (Wing et al., 2020).

In the majority of CRMs, aggregation begins as dry patches form and expand in size. These dry regions get drier while moist regions get moister. The dry patches in these models continue to grow until the convection is constrained to 3–8 quasi-stationary bands orientated along the short axis of the domain. In CM1, SCALE, and WRF-COL-CRM (and DAM to a lesser extent), waves continuously propagate across the domain, taking approximately 3 days to traverse the long axis. These models typically exhibit rapid fluctuations in $\text{var}(\hat{h}_n)$ (Figure 3). Intense convection is generated within these waves, and horizontal humidity variations are smoothed out behind the waves. These waves inhibit aggregation, so these simulations often do not reach the Mature phase. UKMO-CASIM is unique in the way moist regions seem to amplify first in the 295 and 300 K simulations, generating convergence within the moist regions. Dry patches then begin to develop in the divergent regions but they struggle to amplify, often becoming remoistened particularly at warmer SSTs. At 305 K, both the moist and the dry regions in UKMO-CASIM fail to amplify. Not all models reach both the Growth and Mature stages of aggregation at all three SSTs. These models are marked with an asterisk in Figure 3 and do not contribute to model-mean calculations to prevent skewing the results.

Figure 4 shows 24-hr running averages of $\text{var}(\hat{h}_n)$ for each GCM and SST. Also shown are the $\text{var}(\hat{h}_n)$ limits for the Growth and Mature phase of aggregation. All of the GCMs aggregate, again displaying a wide range of characteristics (Wing et al., 2020). Like the majority of CRMs, dry patches develop and expand, while moist regions become moister and increasingly confined until an equilibrium state is reached. Unlike the CRMs, aggregation increases with SST in the majority of GCMs. GCMs that reach a more aggregated state at warmer SSTs do not usually aggregate faster as SST increases, but they tend to continue aggregating for a longer duration.

As with the CRMs, we do not include all GCMs in the model-mean calculations as not all models have data in both the Growth and Mature phases of aggregation for each of the SSTs. These models are marked with an

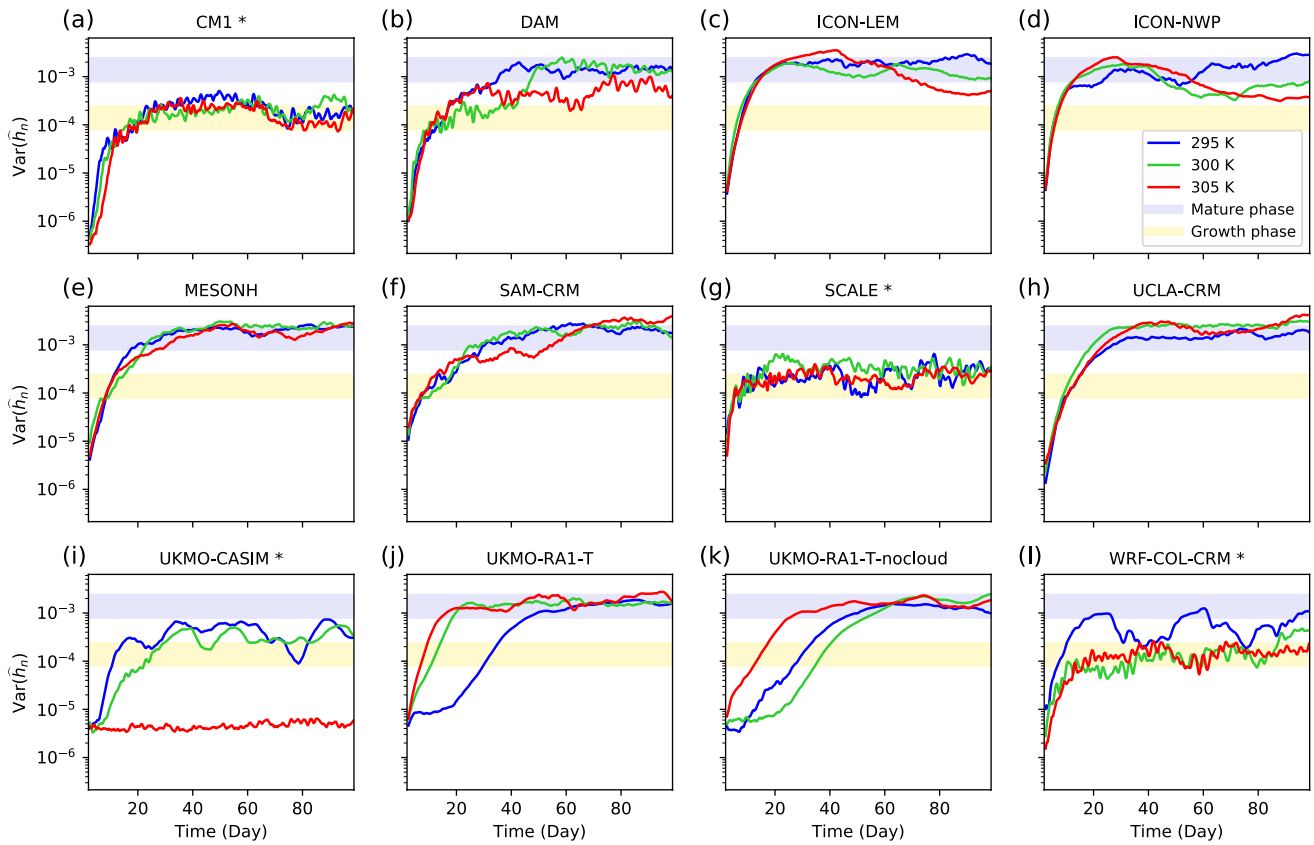


Figure 3. Time series of $\text{var}(\hat{h}_n)$ for each Smoothed Cloud-system Resolving Model and sea surface temperature (SST) neglecting the first 2 days accounting for model spin-up (24-hr running averages). The Growth and Mature phases are indicated by the yellow and blue shaded regions respectively. Models marked with an asterisk (*) are excluded in future model-mean calculations as not all of their simulations reach the Growth and Mature phase for all SSTs.

asterisk in Figure 4. Note CAM5 and CAM6 have FMSE data only for the final 25 days of the 1095-day simulation. ICON-GCM at 300 K already has a variance greater than the upper limit for the Growth phase after 2 days (which we consider the spin-up period) so is not included in model-mean calculations. ECHAM6 and GEOS are included in the model-mean calculations because the 295 K simulations reach the Mature stage after the 100 days shown in Figure 4.

The Growth and Mature thresholds for a given model are fairly arbitrary. So any $\text{var}(\hat{h}_n)$ range which satisfies the criteria of the convection being randomly scattered (Growth) or strongly clustered (Mature) may be used to define the two phases to study any one particular model. However, we want each model to have the same $\text{var}(\hat{h}_n)$ thresholds to make the comparisons in this study as fair as possible. The Growth phase range chosen allows the vast majority of models to be included in the Growth phase. The convection becomes significantly clustered above the upper limit of the Growth phase. Having the lower limit of the Mature phase at 0.8×10^{-3} allows the ECHAM6 and GEOS GCMs to be included, but excludes the CM1, SCALE and UKMO-CASIM CRMs, which do not become “strongly clustered.” Despite all models aggregating to some degree (except UKMO-CASIM at 305 K), we have chosen not to define the Growth and Mature phases relative to the evolution of aggregation within each model because of the extensive range in aggregation among the models. Using Growth and Mature phases defined in that way could result in confusion comparing feedbacks across models because those differences could either be due to changes between the models themselves or due to changes in aggregation. The Growth and Mature definitions used in this study have been chosen in an attempt to make comparisons between the models as fair as possible.

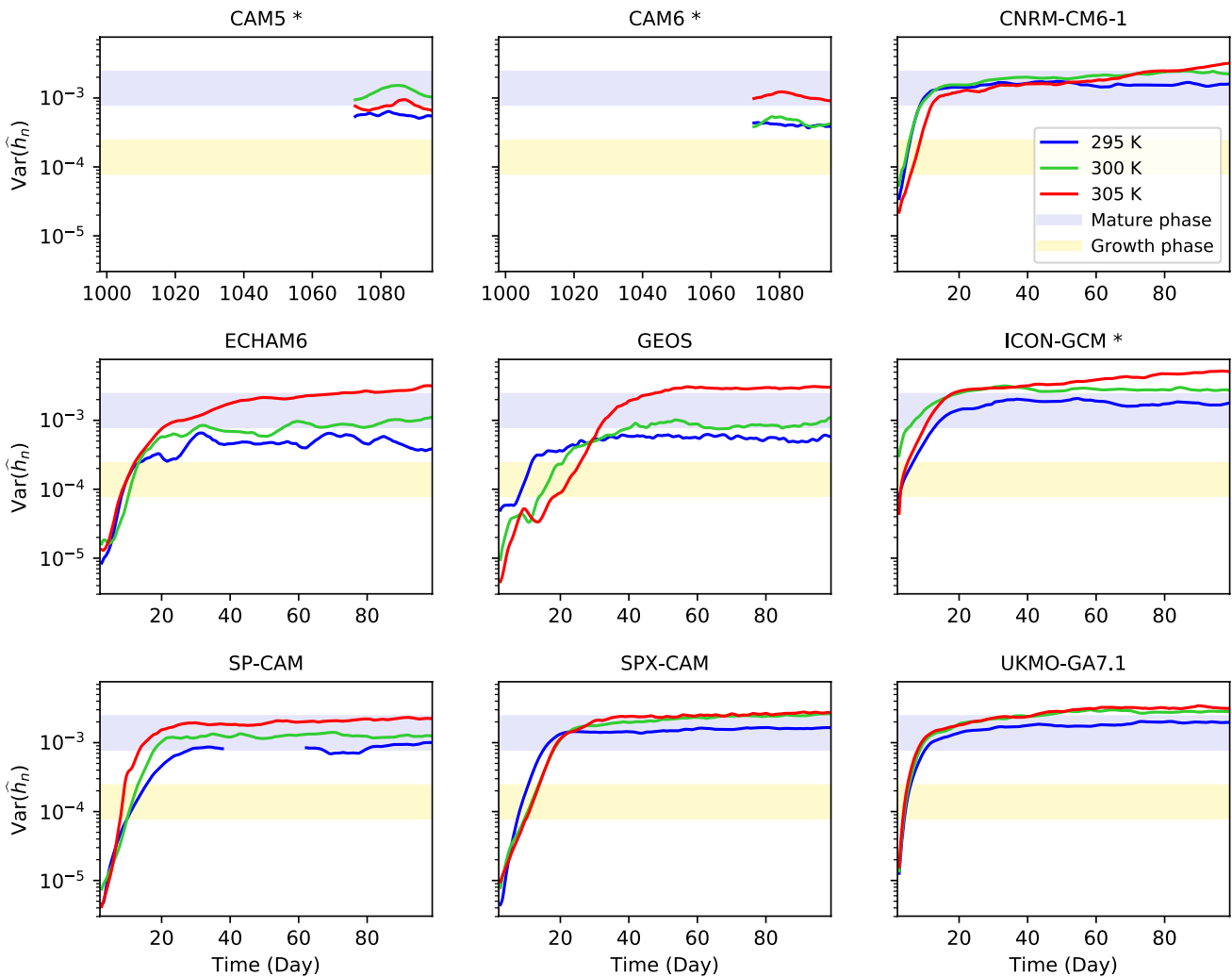


Figure 4. Time series of $\text{var}(\hat{h}_n)$ for each General Circulation Model and sea surface temperature for the first 100 days, neglecting the first 2 days accounting for model spin-up (24-hr running averages). Note that CAM5 and CAM6 only have frozen moist static energy output for the final 25 days of their 1095-day simulations, so we can only analyze that time period for those models. Also note there is missing data for the 295 K SP-CAM simulation from days 37–63 and days 762–800 due to errors in the model output. The Growth and Mature phases are indicated by the yellow and blue shaded regions respectively. Models marked with an asterisk (*) are excluded in future model-mean calculations.

3.2. Normalized FMSE Variance Budget Analysis

Figure 5 shows the spatiotemporal mean of the budget terms during the entirety of the Growth and Mature phase of aggregation for Smoothed CRMs and GCMs and for each SST. From this figure, we can see which FMSE covariances are enhancing or opposing aggregation at these different stages. The $\text{var}(\hat{h}_n)$ tendency is calculated using a second-order finite difference approximation from 6-hourly calculated $\text{var}(\hat{h}_n)$. The diabatic terms are explicitly calculated from hourly-averaged data, whereas the advection term is calculated as a residual of the other terms. This is because the FMSE diagnostic is output as instantaneous values rather than hourly-averaged values for most models that provided it, and FMSE advection is not a diagnostic in all models. By comparing GCMs to the Smoothed CRMs, we remove biases that may be a result of the small-scale features that cannot be resolved in the larger grid spacing in GCMs. Also shown in this figure, are the model-mean longwave and shortwave feedbacks using clear-sky radiation. This allows us to quantify the influence clear-sky radiation on the radiative feedbacks.

Figure 5 shows that for all model types, and at all SSTs, FMSE feedbacks with longwave radiation and surface fluxes are typically the main drivers of aggregation in the Growth phase, however the magnitude of each feedback

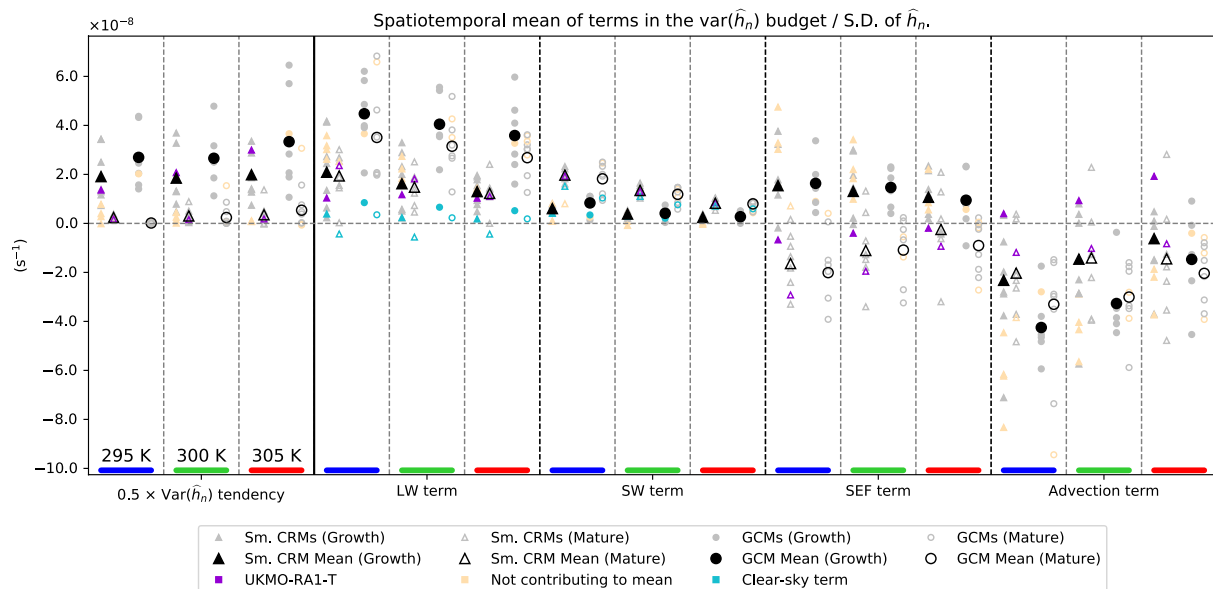


Figure 5. Spatiotemporal mean of terms in the $\text{var}(\hat{h}_n)$ budget equation divided by the instantaneous standard deviation of \hat{h}_n for Smoothed Cloud-system Resolving Models (CRMs) (triangles) and General Circulation Models (GCMs) (circles) at each sea surface temperature (SST) during the Growth phase (filled markers) and Mature phase (open markers) of aggregation. For each term, SST increases to the right. The mean for the Smoothed CRMs and GCMs for each SST are shown in black markers. Models that do not reach both the Growth and Mature phase at all three SSTs are shown with orange markers and do not contribute to the mean. UKMO-RA1-T is shown in purple. Model-mean longwave and shortwave terms using clear-sky radiation are shown in cyan markers.

is highly variable from model to model. The shortwave term is consistently small and positive and has little inter-model variability. The advection term typically opposes aggregation and is the greatest source of variability for the rate of aggregation across the models. The extensive variability in the budget terms highlights that the physical processes affecting aggregation are highly variable from model to model. In addition, the SST dependence of the model mean terms do not represent the SST dependence of the terms in each model. For example, Coppin and Bony (2015) studied the SST dependence of drivers of aggregation in the ISL-CM5A-LR GCM (not in RCEMIP), highlighting that the surface flux term becomes relatively more important as SST increases, in contrast to the RCEMIP model mean terms.

The RCEMIP CRMs that do not contribute to the model mean values are largely those models with waves that rapidly propagate across the domain and smooth horizontal humidity variations (CM1, SCALE, and WRF-COL-CRM). Deep convection occurs in these waves which generate high surface winds. Apparently related to these waves, these models tend to have higher than average longwave and wind-induced surface flux feedbacks, as well as a more negative advection feedback.

During the Mature phase of aggregation, both the longwave and shortwave feedbacks maintain aggregation, and are balanced by the typically-negative surface flux and advection feedbacks. On average, the magnitude of the longwave feedback has little dependence on the degree of aggregation in CRMs, but there is a slight decrease in the majority of GCMs with increased aggregation which is similar in magnitude to the decrease in the clear-sky longwave feedback. The shortwave feedback increases with aggregation as moist and dry regions amplify, leading to larger differences in shortwave absorption between positive and negative \hat{h}_n regions. The surface flux feedback is usually positive during the Growth phase as higher surface wind speeds in moist convective regions leads to a positive feedback. During the mature phase, the wind speed-surface flux feedback becomes overcompensated by the negative air-sea disequilibrium feedback, whereby surface evaporation rates are enhanced in drier environments (Wing & Emanuel, 2014). The surface flux feedback during the Mature phase at higher SSTs may be less negative due to the wind-evaporation feedback being relatively stronger (Coppin & Bony, 2015).

The magnitude of the clear-sky longwave feedback is small in comparison to the total longwave feedback, decreasing slightly as aggregation increases, in agreement with Wing and Cronin (2016). The clear-sky shortwave feedback contributes to a much greater fraction of the total shortwave feedback compared to the clear-sky longwave

feedback. This is because the shortwave feedback is mainly driven by the shortwave absorption by water vapor, which comprises a greater fraction of the total shortwave feedback as SST increases (Pope et al., 2021; Wing & Cronin, 2016; Wing & Emanuel, 2014).

As noted by Wing et al. (2020), GCMs tend to reach a higher degree of aggregation at higher SSTs. With only a slight increase in aggregation rate with SST in GCMs during the Growth phase, aggregation rates increase with SST most significantly for $\text{var}(\hat{h}_n)$ in between the Growth and Mature phases. This can be seen in many of the models in Figure 4. Note that in Figure 5, the $\text{var}(\hat{h}_n)$ tendency of GCMs during the Mature phase continues to increase slightly with SST.

For GCMs during the Growth phase, the sum of the diabatic terms decrease in magnitude with increasing SST, yet the advection term becomes more positive with SST, resulting in a small SST dependence in the rate of aggregation in the Growth phase. After the Growth phase however, the sum of the diabatic feedbacks becomes less SST dependent (because the surface flux feedback becomes more positive with increased SST), while the advection term remains more positive with SST. This results in a greater rate of aggregation after our defined Growth phase. In CRMs, the sum of the diabatic terms also becomes less sensitive to SST after the Growth phase, though they still have a more negative SST dependence than the average of the GCMs. The SST sensitivity of the CRMs' advection feedback tends to oppose the SST sensitivity of their diabatic feedbacks at all stages of aggregation.

The longwave feedback is on average a factor 2 greater in GCMs compared to CRMs for all stages of aggregation. The larger longwave feedback in GCMs is the main difference in terms of the diabatic feedbacks between CRMs and GCMs. This results in GCMs having an overall larger diabatic feedback, corresponding to a more negative advection feedback and/or a higher rate of aggregation in the Growth phase. There is, however, a large spread in the models' advection term and aggregation rate. The difference between the mean advection term between GCMs and Smoothed CRMs is not statistically significant at the 95% confidence level for a given SST, even when including the models that are neglected from the model-mean comparisons. The increase in mean aggregation rate from the Smoothed CRMs to the GCMs is only significant at each SST when we include the models neglected from the model-mean comparisons. The difference in the longwave feedbacks in CRMs and GCMs is significant and will be discussed further in Section 4.2.

There is little difference in the budget terms between the non-Smoothed and Smoothed CRMs (not shown). After dividing the terms by the standard deviation of \hat{h}_n , the rate of aggregation, longwave term, and shortwave term remain similar on average. The most significant difference between the non-Smoothed and Smoothed CRMs is the magnitude of the surface flux term during the Growth phase, which is about 40% smaller in the Smoothed CRMs. We do not have an explanation for why this is. With the surface flux term decreasing in the Growth phase, and the other diabatic terms and $\text{var}(\hat{h}_n)$ tendency term remaining similar, the advection term becomes more positive after smoothing as it is calculated as a residual of the other terms.

If FMSE feedbacks in CRMs and GCMs are represented similarly despite the different grid spacings, the budget terms in GCMs should be similar to the budget terms in the Smoothed CRMs. For both CRMs and GCMs, each of the diabatic terms are typically positive during the Growth phase but on average decrease in magnitude as SST increases (Figure 5). The SST dependence of the radiative terms found here is only in partial agreement with P21, who studied the UKMO-RA1-T model simulations which are represented by the purple, triangular data points in Figures 5, 7, and 8. They analyzed this SST dependence of the UKMO-RA1-T CRM and found the longwave feedback decreases with increasing SST due to the reduction of high-cloud fraction at higher SSTs. However in their study, this SST dependence was only found in the Mature phase. We will explore how high-cloud fraction affects the longwave feedback in the RCEMIP CRMs and GCMs in Section 4. P21 found that the shortwave feedback decreases with increasing SST, and is inversely proportional to the difference between \hat{h}_{\max} and \hat{h}_{\min} . This finding is consistent with the RCEMIP models and physically means that the shortwave heating anomalies contribute similar amounts to increasing the non-normalized FMSE variance at different SSTs. This is because the range of water vapor path (WVP) increases with SST, while the radiative absorption efficiency decreases with increasing WVP (Vaquero-Martínez et al., 2018) resulting in little difference in horizontal net shortwave heating variance with SST. However, since FMSE anomalies are higher at warmer SSTs, the shortwave heating anomalies contribute to a smaller fraction of FMSE variance.

Some of the results from the mean of the models are in contrast to the results found in P21. According to the model means, the surface flux feedback is almost as important as the longwave feedback in driving aggregation,

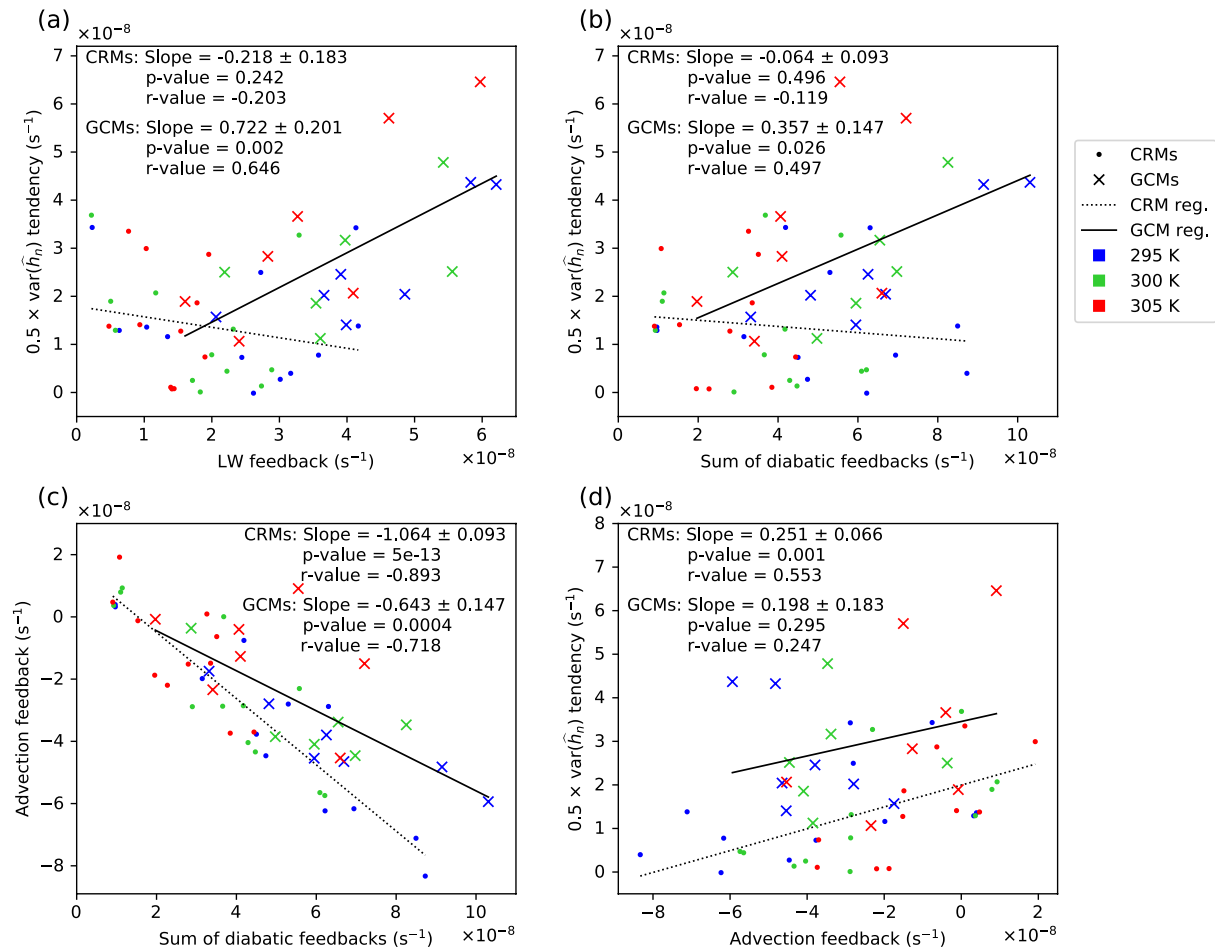


Figure 6. (a) Average of the $\text{var}(\hat{h}_n)$ tendency term versus the longwave term in Equation 5, (b) average of the $\text{var}(\hat{h}_n)$ tendency term versus the sum of the three diabatic terms (longwave, shortwave & surface flux), (c) average of the advection term versus the sum of the diabatic terms, and (d) average $\text{var}(\hat{h}_n)$ tendency term versus the advection term, for each Smoothed Cloud-system Resolving Model (CRM) (points) and General Circulation Model (GCM) (crosses) averaged over the Growth phase. Also shown is the regression line for CRMs (dotted) and GCMs (solid line), as well as their slope, p-value and r-value.

which is in stark contrast to the UKMO-RA1-T model that shows the surface flux feedback to be slightly negative even during the Growth phase. This suggests the air-sea disequilibrium feedback in the UKMO-RA1-T model dominates over the wind speed-surface flux feedback to a larger degree than in the majority of models. The sum of the diabatic terms decreases with increasing SST for the model means, yet it is more constant with SST in the UKMO-RA1-T simulations and is also more negative. Despite the more negative diabatic feedback in UKMO-RA1-T, the rate of aggregation is faster than the model means at 300 and 305 K. This is because the UKMO-RA1-T model has the most positive advection feedback of all models. This feedback increases with SST despite the diabatic terms remaining similar, resulting in faster aggregation at higher SSTs in UKMO-RA1-T. For both CRMs and GCMs in RCEMIP, the advection term is inversely proportional to the sum of the diabatic terms, becoming less negative with increasing SST. The result is that the rate of aggregation during the Growth phase for both CRMs and GCMs does not depend very strongly on SST.

Previous literature has shown the diabatic terms to be essential drivers of aggregation, so we would expect that a greater diabatic-FMSE feedback would lead to an increased rate of aggregation. Despite the diabatic terms driving aggregation in the Growth phase of the RCEMIP simulations (Figure 5), we cannot conclude that the magnitude of the sum of the diabatic terms is correlated to the rate of aggregation. Figure 6a shows the correlation between the longwave term and the $\text{var}(\hat{h}_n)$ tendency term in Equation 5 during the Growth phase for Smoothed CRMs and GCMs. We find there is a significant correlation between the longwave term and rate of aggregation in the GCMs, but there is no significant correlation between the longwave term and rate of aggregation in the

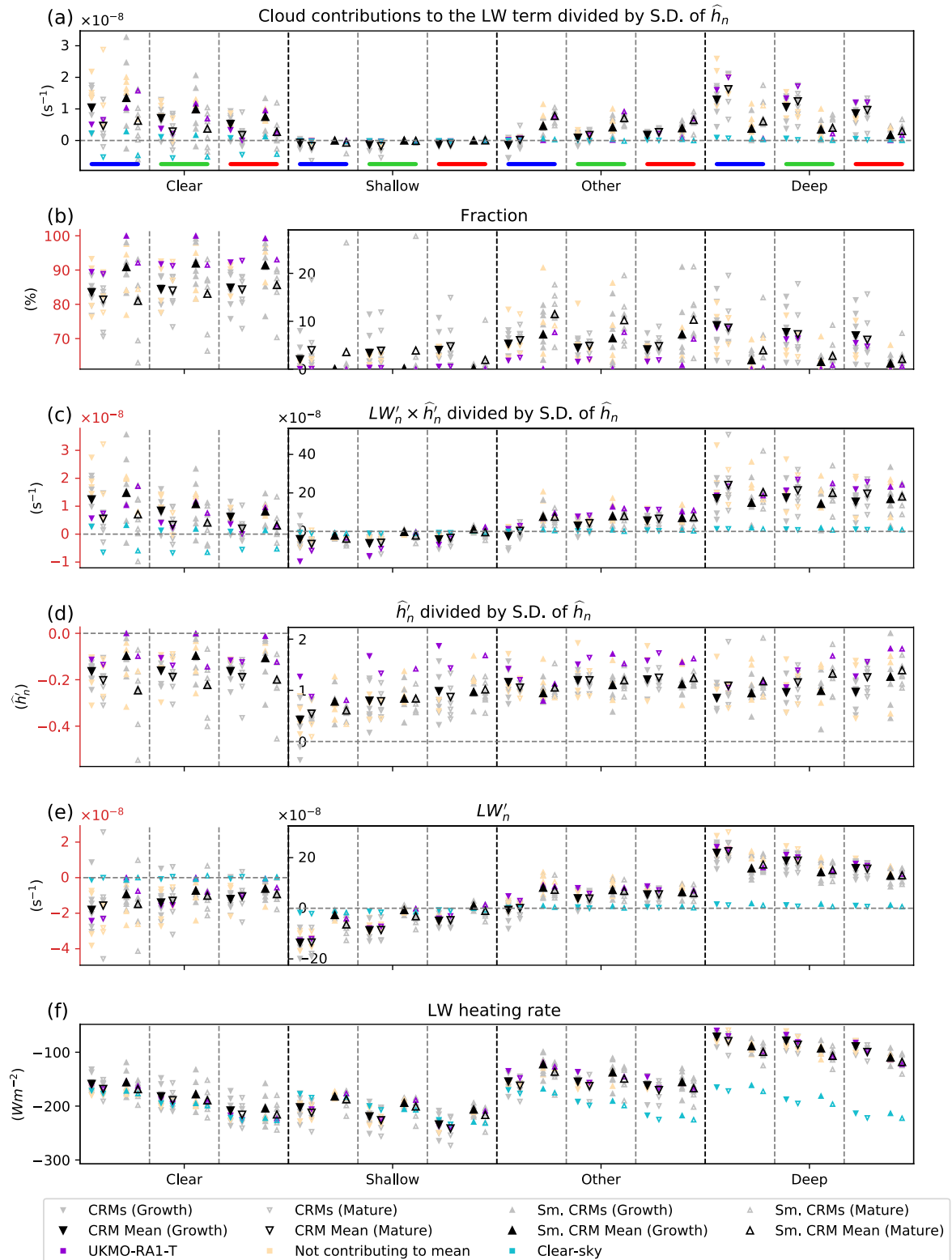


Figure 7. Cloud-system Resolving Models (CRMs) (downward triangles) versus Smoothed CRMs (upward triangles): (a) Contributions of longwave interactions for each cloud type in Table 1 to the longwave term in Equation 5 (equal to the cloud type fraction multiplied by their mean $LW'_n \times \hat{h}'_n$ covariance) divided by the standard deviation of \hat{h}_n , (b) cloud type fraction, (c) $LW'_n \times \hat{h}'_n$ covariance divided by the standard deviation of \hat{h}_n , (d) \hat{h}'_n divided by the standard deviation of \hat{h}_n , (e) LW'_n , and (f) net longwave heating (Equation 3). Data points represent spatiotemporal means. The layout follows the same protocol as Figure 5. Note different y-axis ranges for Clear in (b, c, d, and e).

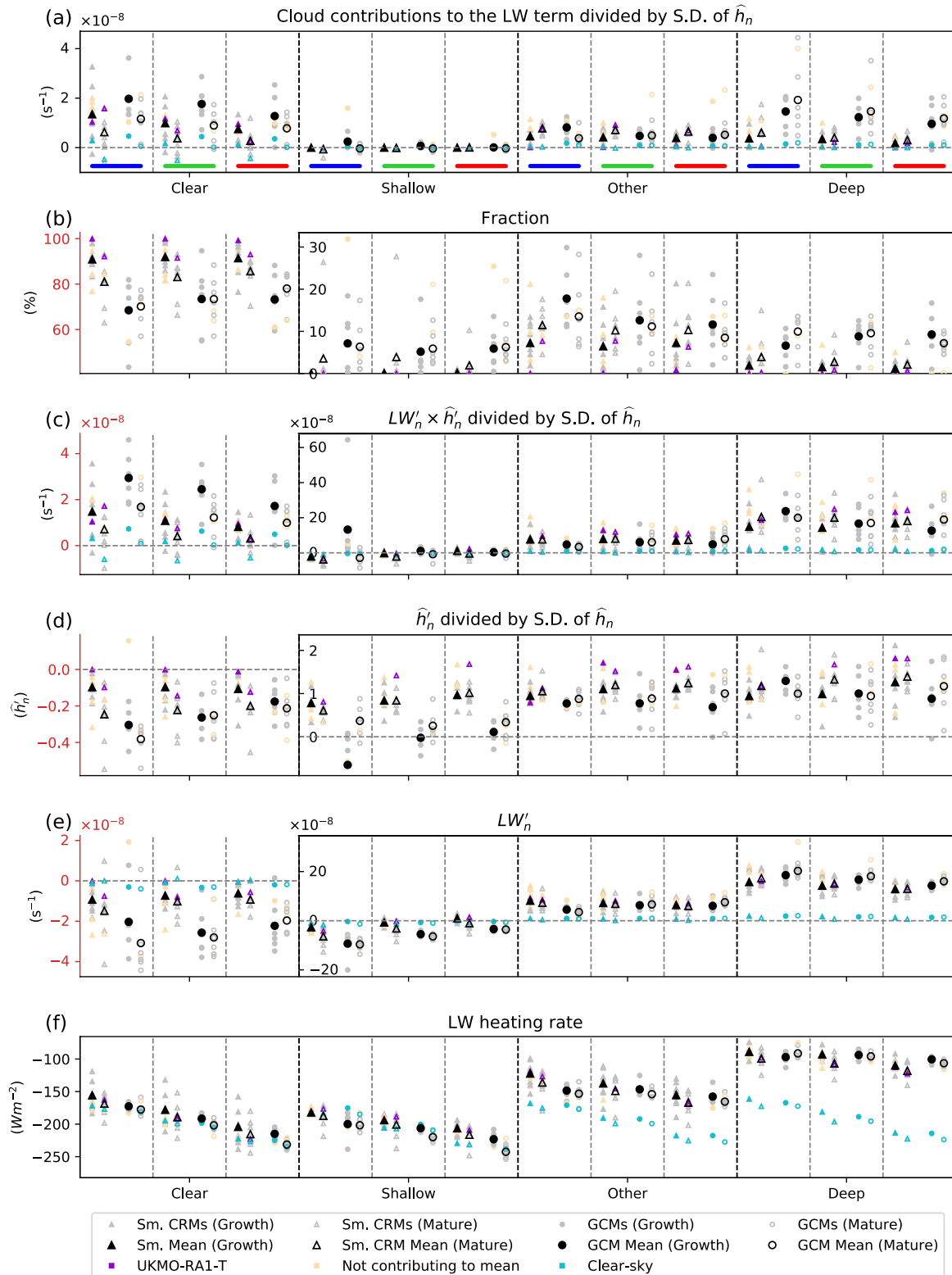


Figure 8. Smoothed Cloud-system Resolving Models (upward triangles) versus General Circulation Models (circles): (a) Contributions of longwave interactions for each cloud type in Table 1 to the longwave term in Equation 5 (equal to the cloud type fraction multiplied by their mean $LW'_n \times \hat{h}_n$ covariance) divided by the standard deviation of \hat{h}_n , (b) cloud type fraction, (c) $LW'_n \times \hat{h}_n$ covariance divided by the standard deviation of \hat{h}_n , (d) \hat{h}_n divided by the standard deviation of \hat{h}_n , (e) LW'_n , and (f) net longwave heating (Equation 3). Data points represent spatiotemporal means. The layout follows the same protocol as Figure 5. Note different y-axis ranges for Clear in (b, c, d, and e).

CRMs (regardless of Smoothing). Figure 6b shows the correlation between the sum of the diabatic terms and the $\text{var}(\hat{h}_n)$ tendency term. Again there is a significant positive correlation between the diabatic feedbacks and rate of aggregation in the GCMs, but not for the CRMs. A greater diabatic feedback is associated with a more negative advection feedback (Figure 6c). In the CRMs, the sum of the diabatic terms is, on average, proportional to the magnitude of the advection feedback, hence there is no significant relationship between the diabatic feedbacks and aggregation rate. There is a less negative relationship between the sum of the diabatic terms and the advection term in the GCMs, allowing GCMs with a higher diabatic feedback to aggregate faster. The rate of aggregation in CRMs is most strongly correlated with the advection feedback (Figure 6d), with no significant correlation between the advection feedback and aggregation rate in the GCMs.

The longwave feedback is one of the key drivers and maintainers of aggregation in the majority of models at each SST. It is typically a larger feedback in GCMs, resulting in largely faster aggregation rates compared to CRMs. The longwave feedback is a major factor in determining the model spread in the rate of aggregation in GCMs. We explore the contributions of different cloud-radiation interactions to the longwave feedback in the following section. We assess their SST sensitivities, and compare and contrast CRMs and GCMs.

4. Contributions of Cloud-Radiation Interactions to Aggregation

In this section, we compare longwave-cloud interactions within the CRMs and GCMs. We first study these interactions in the CRMs to test the robustness of the conclusions in P21. We then compare CRMs to GCMs by first seeing how cloud-longwave interactions are affected by coarsened grid spacing using the Smoothed CRMs. Then we compare the Smoothed CRMs to GCMs to study why the longwave feedback tends to be stronger in GCMs.

4.1. Cloud-Radiation Interactions Within CRMs

The contributions to aggregation from longwave interactions with each of the cloud types in Table 1 for CRMs and Smoothed CRMs are shown in Figure 7a, comparing SST and phase of aggregation. Each model that contributes to the mean is shown in gray, the model mean shown in black, UKMO-RA1-T is shown in purple, and models that do not contribute to the mean are shown in light orange. The model-mean contributions to the longwave term using clear-sky radiation are shown in the cyan points. We first focus on the (non-Smoothed) CRMs.

There is great variability between the models in terms of cloud fraction, and the LW' and \hat{h}_n' of the different cloud types, so the factors affecting the longwave feedback vary considerably from model to model. However, for the CRMs during the Growth phase of aggregation, longwave interactions with the Clear and Deep regions typically contribute most to the longwave feedback. The Clear regions have a large contribution mainly because of their large domain-fraction (Figure 7b) and positive $LW'_n \times \hat{h}_n'$ covariance (Figure 7c), despite the covariance being on average the lowest in magnitude out of all cloud types. Deep clouds are the next most abundant cloud type on average and typically have the largest $LW'_n \times \hat{h}_n'$ covariance of all cloud types. They have the largest LW'_n due to their cold cloud tops (Figure 7e) and have the second highest \hat{h}_n' of the cloud types (Figure 7d). A large portion of the Deep category comes from thin anvil cloud which often extend a great distance from the high-FMSE updraft that they originated from. This transport of high cloud to lower-FMSE regions lowers the average \hat{h}_n' of the Deep category. The Shallow and Other cloud types have an insignificant contribution to the longwave feedback in comparison because their $LW'_n \times \hat{h}_n'$ covariance is small in magnitude (mostly due to a small-magnitude LW'_n) and they have a small fraction (although the fraction is highly variable between models).

The negative SST dependence of the longwave feedback, as seen in Figure 5, can be explained by the negative SST dependence of the longwave interactions with the Deep and Clear regions as follows, in agreement with P21. During both the Growth and the Mature phases, the $LW'_n \times \hat{h}_n'$ covariance of the Deep regions remains similar with SST (Figure 7c) while the Deep cloud fraction steadily decreases (Figure 7b), so the SST dependence of the Deep cloud's longwave contribution to aggregation is primarily due to the decrease in Deep cloud fraction.

The contribution of the Clear regions decreases with increasing SST due to the decrease in the Clear $LW'_n \times \hat{h}_n'$ covariance. We do not find the clear-sky longwave feedback in the Clear regions decreasing with SST by the same extent, indicating that the SST sensitivity of the Clear regions' longwave feedback is a side effect of the cloud response to SST. There are multiple factors that influence this SST dependence: the change in longwave heating

rates of the different cloud types, the change in their fraction, the increase in the range of \hat{h}_{\max} and \hat{h}_{\min} , and the change in correlation between longwave and FMSE anomalies in the Clear regions. The correlation between LW'_n and \hat{h}'_n remains similar with SST (15% decrease in the correlation coefficient from 0.173 at 295 K to 0.147 at 305 K), as does the mean \hat{h}'_n (Figure 7d). The change in the Clear $LW'_n \times \hat{h}'_n$ covariance is therefore mainly due to the change in Clear LW'_n .

To isolate the effects of the changing longwave heating rates with SST on the Clear longwave feedback, we use the average cloud type fractions at 295 K with the average cloud type longwave heating rates at 305 K. By taking the sum of the product of these cloud fractions and their longwave heating rates, we calculate a hypothetical new domain-mean longwave heating rate. Then a new hypothetical LW' for each cloud type is calculated by subtracting the new domain-mean heating rate from the cloud type net longwave heating rates. We find that the average Clear LW' becomes 74% more negative compared to the values at 295 K. However, after normalizing LW' to account for the changing SST, we find this hypothetical new Clear LW'_n is largely insensitive to SST. We next isolate the effect of the changing cloud fraction with SST by using the average cloud type longwave heating rates at 295 K with the average cloud type fractions at 305 K to calculate the cloud types' LW' . We find the domain-mean longwave cooling rate increases by approximately 3 W m^{-2} compared to the value at 295 K, and is mainly a result of the decreasing Deep cloud fraction allowing for enhanced radiative cooling. The increased domain-mean cooling rate is closer to the mean cooling rate of the Clear regions, making their LW' 37% less anomalously negative. This is close to the actual 30% decrease in the mean LW'_n of the Clear regions. This shows that the SST sensitivity of the Clear LW'_n is primarily due to changes in cloud fraction with SST.

The contribution of the clear-sky longwave feedback to the total feedback is negligible in the cloudy regions (Figure 7a). This is because the clear-sky longwave heating anomalies are much smaller than the total longwave heating anomalies (Figure 7e), showing that the longwave feedback is mainly a result of the longwave interactions with clouds. Even the Clear regions' longwave contribution is more positive than the clear-sky feedback because the longwave anomalies in Clear regions are more anomalously negative within a domain containing clouds.

For the Clear regions, the decrease in their longwave feedback with increasing aggregation is largely a clear-sky effect, with their total longwave feedback and their clear-sky longwave feedback decreasing by a similar magnitude (Figures 7a and 7c). On average, the Clear regions' LW'_n remains similar with aggregation (becoming very slightly more positive) and their \hat{h}'_n becomes more negative. But the changes in these model-mean values are not enough to explain the decrease in the mean $LW'_n \times \hat{h}'_n$ covariance in the Clear regions. The decrease in this covariance must be due to a decrease in the correlation between LW'_n and \hat{h}'_n as aggregation increases, which is a clear-sky radiation effect. During the Growth phase, there is a positive correlation between \hat{h}'_n and clear-sky LW'_n . This is because regions with increasingly positive \hat{h}'_n have a greater column-integrated WVP, thus a higher effective level of OLR emission, reduced OLR (Allan et al., 1999), and therefore a higher LW' . During the Mature phase, there is a greater abundance of extremely dry regions. In these extremely dry regions, an increase in WVP more readily lowers the effective emission level of downwelling longwave radiation (Ruckstuhl et al., 2007) than increases the effective emission level of OLR (Figure S4 in P21). The consequence is increasingly negative LW' at higher \hat{h}'_n . This is a negative correlation, and helps to make the total Clear longwave feedback more negative in the Mature phase. The transition of the driest regions' clear-sky longwave feedback from initially positive to negative as aggregation increases is also described by Wing and Emanuel (2014), who explain it as a competition between local and remote effects using a simple two-layer model.

Next, we look at the effects of smoothing on cloud-longwave interactions in the CRMs to see how a coarser grid spacing affects cloud-longwave interactions. After smoothing the TOA radiative fluxes and reclassifying the cloud types using the smoothed radiation, there is a large difference in the fraction of the different cloud types (Figure 7b). First, there is an almost complete elimination of Shallow cloud in the Smoothed CRMs during the Growth phase, with a large reduction in Deep cloud in the Growth and Mature phases. This is because the Shallow and Deep clouds are often small in area, particularly during the Growth phase, meaning that after averaging the TOA radiative fluxes across the surrounding $120 \times 120 \text{ km}$ area, these clouds are often reclassified as either Clear or Other clouds. This results in an increase in Other cloud, although there is an approximate halving of the total cloud fraction during the Growth phase. During the Mature phase, all cloud types increase in fraction in the Smoothed CRMs as a likely result from increased cloud clustering. The total cloud fraction in the Mature phase is similar to the non-Smoothed CRMs.

Smoothing also has an effect on the average $LW'_n \times \hat{h}'_n$ covariance of the cloud types (Figure 7c). The covariance remains similar for Deep cloud, but increases slightly for the Other cloud, perhaps a result of a significant proportion of the non-Smoothed Deep cloud regions becoming reclassified as Other after Smoothing, as can be inferred by comparing Figures 2a and 2b. The combined effects of the change in cloud fraction and $LW'_n \times \hat{h}'_n$ covariance after Smoothing is a reduction in the contribution from Deep cloud with subsequent increases in the contributions from the Other and Clear cloud types during all stages of aggregation. Smoothing has a negligible effect on the clear-sky longwave feedback.

4.2. Comparison of Cloud-Radiation Interactions Within CRMs and GCMs

In Figure 8, we compare the longwave-cloud interactions between the Smoothed CRMs and GCMs. Figure 8a shows that during the Growth phase, longwave interactions with the Clear regions and Deep regions are the main drivers of aggregation for GCMs, with interactions with Other clouds also having a significant contribution. Contributions of each of these cloud types to the total longwave feedback are higher in GCMs compared to the Smoothed CRMs. This is largely due to the increased fraction of the Other and Deep cloud types (Figure 8b), but also the increased $LW'_n \times \hat{h}'_n$ covariance of the Deep and Clear cloud types (Figure 8c).

The absolute net longwave heating rate (defined in Equation 3) of Deep cloud is similar in the Smoothed CRMs and GCMs, but in the Clear regions, the longwave heating rate is more negative on average for GCMs (Figure 8f). Given that the clear-sky longwave heating rate in the Clear regions is similar in CRMs and GCMs, the decreased longwave cooling in CRMs is likely a result of more thin high cloud being present in the Clear regions. Since Clear regions occupy the majority of the domain, the domain-mean longwave emission is closely linked to that of the Clear regions. This makes the Deep clouds in GCMs have a more positive LW'_n (Figure 8e), helping increase their $LW'_n \times \hat{h}'_n$ covariance.

The $LW'_n \times \hat{h}'_n$ covariance of the Clear regions is more than double that of the Smoothed CRMs. This is in part because Clear regions in GCMs typically occur in more negative \hat{h}'_n compared to Smoothed CRMs (Figure 8d), which is a likely consequence of the greater cloud fraction in GCMs, confining the Clear regions to drier environments. The LW'_n is also more negative in GCMs partially due to the mean net longwave heating rates being more negative on average, but mainly because of the difference in cloud fraction between the model types. To isolate the effect of the difference in cloud fraction between CRMs and GCMs on the Clear regions' longwave feedback, we use the mean longwave heating rates of the cloud types in the Smoothed CRMs with the cloud fractions of the GCMs. We then calculate a hypothetical new domain-mean longwave cooling by taking the sum of the product of these cloud fractions and net longwave heating rates and then find the new hypothetical cloud type LW' . We find that the LW'_n of the Clear regions becomes approximately 2.5 times more negative. This is thanks to the Deep and Other clouds lowering the domain-mean longwave cooling rate in GCMs, hence making the Clear regions more anomalously negative. These effects suggest that the greater high-topped cloud fraction in GCMs is a key factor in the enhanced total longwave-FMSE feedback, and therefore rate of aggregation in GCMs compared to CRMs. The non-Smoothed CRMs have a similar Deep cloud fraction and Deep $LW'_n \times \hat{h}'_n$ covariance to the GCMs, yet the contributions from Other and Clear cloud types remain larger in GCMs thanks to the increase in the Other cloud fraction in GCMs. The increase in Other cloud fraction, with their positive LW' , helps further lower the (negative) LW' of the Clear regions in GCMs compared to non-Smoothed CRMs, helping increase these cloud types' contributions to the longwave feedback.

As the convection reaches the Mature phase, longwave interactions in the Clear, Other and Deep cloud types maintain aggregation in the Smoothed CRMs. For GCMs, longwave interactions with the Clear and Deep cloud types are the key maintainers of aggregation. The contribution from the Clear regions decreases with aggregation in both the CRMs and GCMs because of the clear-sky effect described in Section 4.1. Despite the GCMs having a larger Shallow fraction, these clouds have a similarly insignificant contribution to the longwave feedback as in the Smoothed CRMs. Their $LW'_n \times \hat{h}'_n$ covariance is consistently close to 0 because both their LW'_n and \hat{h}'_n are small.

The SST sensitivity of the longwave feedback in GCMs is less straightforward than CRMs with multiple factors playing a role. As with the CRMs, there is great variability between the models in the factors affecting the longwave feedback. On average, during the Growth and Mature phases, the longwave feedback decreases with increasing SST because of a decrease in the contributions from the Clear and Deep categories. The decrease in

the contributions from Clear regions comes from their decreasing $LW'_n \times \hat{h}'_n$ covariance. During both phases of aggregation, the Clear \hat{h}'_n becomes less negative, which is in part a result of the decreased Deep and Other cloud fraction. These clouds form in anomalously positive \hat{h}'_n regions, so a decrease in their abundance with increasing SST will result in an increase in anomalously moist Clear regions, thus decreasing the mean Clear $LW'_n \times \hat{h}'_n$ covariance. The main factors responsible for the decreasing contribution from Deep cloud is the increase in the range of \hat{h}_{\max} and \hat{h}_{\min} that is used to normalize the longwave heating anomalies, as well as a decrease in their average \hat{h}'_n in the Growth phase.

5. Conclusions

In this study, we compare the effects of cloud-radiation interactions on convective self-aggregation within the CRMs and GCMs submitted to RCEMIP (Wing et al., 2018, 2020). We use the normalized vertically-integrated FMSE variance ($\text{var}(\hat{h}_n)$) budget framework to study aggregation (Pope et al., 2021, referred to as P21.), and define “Growth” and “Mature” phases of aggregation to compare how FMSE feedbacks contribute to aggregation at similar stages of aggregation across the range of models. We define four different cloud types based on the TOA radiative fluxes following the method from Becker and Wing (2020) and calculate the contribution of radiative interactions with these cloud types to aggregation. These cloud types are: Clear, Shallow, Deep and Other. GCMs have on average a 40 times larger grid spacing than CRMs. When comparing these two model types we account for biases in our analysis technique due to the resolution difference by horizontally smoothing the CRMs so that each grid point is an average of the 40×40 grid points surrounding it, referred to as Smoothed CRMs.

The goals of the study are to:

- Validate the robustness of the results in P21 who studied the effects of cloud-radiation interactions on self-aggregation within the Met Office Unified Model version 11.0 CRM (submitted to RCEMIP and referred to as “UKMO-RA1-T”).
- Investigate to what extent differences in cloud-radiation interactions affect self-aggregation within CRMs and GCMs, and how these are sensitive to SST.

5.1. Robustness of P21 Results

We consider the robustness of the following five conclusions from P21:

1. Key *drivers* of aggregation are longwave interactions with high-topped clouds and Clear regions. (*Robust*)
Most CRMs and GCMs are in agreement with this conclusion when considering that Deep cloud are mostly equivalent to high-topped clouds in P21. Deep clouds have strong longwave heating anomalies and occur in anomalously moist regions. Clear regions typically have negative longwave heating anomalies and tend to occur in anomalously dry regions. Both of these radiative interactions result in a strongly positive longwave feedback.
2. The main *maintainers* of aggregation are longwave interactions with high-topped clouds and shortwave interactions with water vapor. (*Robust*)
Most CRMs and GCMs are in agreement that these radiative interactions are key maintainers of aggregation. The shortwave feedback increases with aggregation as moist and dry regions amplify, leading to a greater contrast in shortwave absorption by water vapor between the moist and dry regions, resulting in an enhanced shortwave-FMSE feedback.
3. The main *resistors* of aggregation are negative surface flux and advection feedbacks. (*Not Robust for surface flux in the Growth phase*)
In the majority of models, the surface flux feedback is actually a key *driver* of aggregation, with the UKMO-RA1-T model having the most negative surface flux contribution during the Growth phase. In most models, this is likely due to a strong wind speed-induced surface flux feedback outweighing the air-sea disequilibrium feedback during the Growth phase of aggregation (unlike in UKMO-RA1-T where the opposite is true). As aggregation matures, the models are in agreement that the surface flux feedback becomes increasingly negative and often opposes aggregation. The advection feedback is typically negative and highly variable between models.
4. The *SST-dependence* of the longwave feedback is absent during the Growth phase, but is negative in the Mature phase. (*Not Robust for Growth phase*)

For the RCEMIP models, the domain-mean longwave feedback decreases with increasing SST at *all stages* of aggregation, which is primarily due to the decrease in Deep and/or Other cloud fraction at warmer SSTs. P21 also find the high-topped cloud fraction decreases with increasing SST, however this is compensated by an increase in their mean longwave-FMSE covariance in the Growth phase. We do not find the longwave-FMSE covariance of the Deep and Other clouds increasing with SST in the majority of RCEMIP models, hence their domain mean longwave feedback tends to decrease with SST.

The RCEMIP CRMs and GCMs differ in the processes leading to the decrease in the longwave feedback with increasing SST. For the CRMs, the average longwave-FMSE covariance of these clouds remains similar with SST, so the decrease in their cloud fraction reduces their total aggregating influence. A secondary effect of the decreased Deep cloud fraction is an increase in the magnitude of domain mean longwave cooling. This makes the typically-negative longwave heating anomalies of the Clear regions less anomalous, also decreasing the Clear regions' aggregating influence at warmer SSTs. In GCMs, the longwave feedback decreases with SST because the normalized longwave heating anomalies of Deep clouds decreases, reducing their aggregating influence. In addition, the Clear regions occur in less anomalously dry regions due to the reduced total cloud fraction, also reducing their average aggregating influence as SST increases.

5. The SST-dependence of the aggregation rate is positive because the advection feedback becomes increasingly positive with SST. (*Not Robust for SST-dependence of the aggregation rate. Robust for the SST-dependence of the advection feedback*)

P21 find the sum of the diabatic feedbacks are insensitive to SST during the Growth phase, however for the RCEMIP CRMs and GCMs, each diabatic feedback tends to decrease with increasing SST during the Growth phase. Despite the sum of these diabatic feedbacks decreasing with SST, the rate of aggregation remains similar on average. The sum of the diabatic feedbacks tends to be proportional to the magnitude of the (negative) advection feedback, resulting in little change in aggregation rate with SST.

5.2. Differences Between GCMs and CRMs

Using $\text{var}(\hat{h}_n)$ as our aggregation metric, we find there is much variability in the rate of aggregation and the maximum degree of aggregation within the CRMs, with no consistent SST dependence on the rate of aggregation and the maximum degree of aggregation. GCMs, on the other hand, aggregate faster than CRMs on average, and tend to be more aggregated at higher SSTs.

Both the contributions of shortwave-FMSE and surface flux-FMSE feedbacks to aggregation are similar in magnitude in Smoothed CRMs and GCMs. However, the longwave-FMSE feedback is, on average, approximately twice as strong in GCMs compared with CRMs. This results in typically faster rates of aggregation in GCMs. This is primarily due to GCMs having a larger cloud fraction than Smoothed CRMs, but more crucially a larger Deep cloud fraction. However, if GCMs are instead compared to the non-Smoothed CRMs, GCMs have a similar Deep fraction but a larger Other fraction, which still results in a greater total longwave-FMSE feedback. The longwave-FMSE feedback is strongest for Deep clouds because they typically occur in anomalously-high FMSE regions, and have anomalously strong positive longwave heating rates. Like with the SST sensitivity of cloud fraction in CRMs, a secondary effect of the increased Deep cloud fraction in GCMs is an increase in the longwave-FMSE feedback in the Clear regions. This is because an increased cloud fraction reduces the magnitude of domain-mean longwave cooling. With Clear regions occupying the majority of the domain, their typically-negative longwave heating anomalies become more negative, increasing their longwave-FMSE feedback. The increase in the contributions from Deep and Clear regions to the longwave-FMSE feedback accounts for the doubling of the total feedback.

As previously mentioned, the sum of the diabatic feedbacks with FMSE tend to decrease with increasing SST during the Growth phase, yet the aggregation rate remains insensitive to SST thanks to the increasingly positive advection feedback. After the Growth phase however, the sum of the diabatic feedbacks becomes less SST dependent, yet the advection feedback remains more positive at higher SSTs in GCMs, resulting in GCMs being more aggregated at higher SSTs. This finding, and the point made above about differences in cloud amount between GCMs and CRMs, suggests that GCMs should be compared more systematically to CRMs to investigate their total cloud amount.

Despite the difference in the diabatic feedbacks between GCMs and CRMs accounting for the difference in the aggregation rate between these model types, there is no evidence that the model spread in the magnitude of the

diabatic feedbacks can explain the model spread in the rate of aggregation in CRMs. On average for CRMs, the magnitude of the (negative) advection feedback is proportional to the sum of the diabatic feedbacks. The advection term may be largely influenced by deep overturning circulations that transport FMSE from moist to dry regions, dampening aggregation. The rate of aggregation in CRMs is most strongly correlated with the magnitude of the advection term. Unlike in CRMs, the diabatic feedbacks are significantly correlated with aggregation rate in GCMs. This may suggest that the overturning circulations that smooth horizontal humidity gradients are relatively weaker compared to the diabatic feedbacks in GCMs than CRMs. One possibility is that GCMs are not capturing key circulations that would otherwise mediate aggregation, although circulations in CRMs could also be too strong. These effects are not investigated in this study.

We have shown that the production of cloud in CRMs and GCMs, in terms of quantity and distribution, is very different. This in turn, results in largely different longwave-FMSE feedbacks that alter the rate and degree of aggregation. Not only are the longwave-FMSE interactions enhanced in GCMs, but there is a less negative correlation between the diabatic and advection feedbacks in GCMs than CRMs. This suggests that the response of circulations to diabatic heating are different in GCMs and CRMs. These factors highlight our limitations to accurately represent the cloud response to warming in climate studies. CRMs are often used to study the cloud response to warming, but are too small to capture the large-scale circulations that affect the total cloud feedback. GCMs are used in climate modeling studies because they are complete representations of the climate system, and they can perform hundreds of years of global-scale simulations. However, there are discrepancies in cloud-radiation interactions and circulations between GCMs and CRMs. Both CRMs and GCMs should be evaluated against observations in an effort to make these aspects of clouds and circulations more realistic.

Data Availability Statement

We thank the German Climate Computing Center (DKRZ) for hosting the standardized RCEMIP data, which is publicly available at <http://hdl.handle.net/21.14101/d4bee8e-6996-453e-bbd1-ff53b6874c0e>. Animations of normalized FMSE for all models, plus data used for plotting each figure and the original python scripts are available on Zenodo at: <https://doi.org/10.5281/zenodo.7338001>.

Acknowledgments

This work was supported by the Natural Environment Research Council SCENARIO DTP (NE/L002566/1). The simulations of the UKMOi-vn1.0-RA1-T model have been produced by Todd Jones, supported by the Natural Environment Research Council (NERC) under the joint NERC/Met Office ParaCon program's Circle-A project (NE/N013735/1), as well as the ParaCon Phase 2 project: Understanding and Representing Atmospheric Convection across Scales (NE/T003871/1). The simulations have been conducted using Monsoon2, a High Performance Computing facility funded by the Met Office and NERC, the NEXCS High Performance Computing facility funded by NERC and delivered by the Met Office, and JASMIN, the UK collaborative data analysis facility. The authors thank Allison Wing and another reviewer for their insightful feedback on the manuscript.

References

- Allan, R. P., Shine, K. P., Slingo, A., & Pament, J. A. (1999). The dependence of clear-sky outgoing long-wave radiation on surface temperature and relative humidity. *Quarterly Journal of the Royal Meteorological Society*, 125(558), 2103–2126. <https://doi.org/10.1002/qj.49712555809>
- Arnold, N. P., & Randall, D. A. (2015). Global-scale convective aggregation: Implications for the Madden-Julian oscillation. *Journal of Advances in Modeling Earth Systems*, 7(4), 1499–1518. <https://doi.org/10.1002/2015MS000498>
- Becker, T., & Wing, A. (2020). Understanding the extreme spread in climate sensitivity within the Radiative-Convective Equilibrium Model Intercomparison Project. *Journal of Advances in Modeling Earth Systems*, 12(10), e2020MS002165. <https://doi.org/10.1029/2020MS002165>
- Bony, S., Semie, A., Kramer, R. J., Soden, B., Tompkins, A. M., & Emanuel, K. A. (2020). Observed modulation of the tropical radiation budget by deep convective organization and lower-tropospheric stability. *AGU Advances*, 1(3), e2019AV000155. <https://doi.org/10.1029/2019AV000155>
- Bony, S., Stevens, B., Coppin, D., Becker, T., Reed, K. A., Voigt, A., & Medeiros, B. (2016). Thermodynamic control of anvil cloud amount. *Proceedings of the National Academy of Sciences of the United States of America*, 113(32), 8927–8932. <https://doi.org/10.1073/pnas.1601472113>
- Bretherton, C. S., Blossey, P. N., & Khairoutdinov, M. (2005). An energy-balance analysis of deep convective self-aggregation above uniform SST. *Journal of the Atmospheric Sciences*, 62(12), 4273–4292. <https://doi.org/10.1175/JAS3614.1>
- Chen, Y.-T., & Wu, C.-M. (2019). The role of interactive SST in the cloud-resolving simulations of aggregated convection. *Journal of Advances in Modeling Earth Systems*, 11(10), 3321–3340. <https://doi.org/10.1029/2019MS001762>
- Coppin, D., & Bony, S. (2015). Physical mechanisms controlling the initiation of convective self-aggregation in a General Circulation Model. *Journal of Advances in Modeling Earth Systems*, 7(4), 2060–2078. <https://doi.org/10.1002/2015MS000571>
- Held, I. M., Helmer, R. S., & Ramaswamy, V. (1993). Radiative-convective equilibrium with explicit two-dimensional moist convection. *Journal of the Atmospheric Sciences*, 50(23), 3909–3927. [https://doi.org/10.1175/1520-0469\(1993\)050<3909:RCEWET>2.0.CO;2](https://doi.org/10.1175/1520-0469(1993)050<3909:RCEWET>2.0.CO;2)
- Holloway, C. E., Wing, A. A., Bony, S., Muller, C., Masunaga, H., L'Ecuyer, T. S., et al. (2017). Observing convective aggregation. *Surveys in Geophysics*, 38(6), 1199–1236. <https://doi.org/10.1007/s10712-017-9419-1>
- Jeevanjee, N., & Romps, D. M. (2013). Convective self-aggregation, cold pools, and domain size. *Geophysical Research Letters*, 40(5), 994–998. <https://doi.org/10.1002/grl.50204>
- Muller, C., & Held, I. M. (2012). Detailed investigation of the self-aggregation of convection in cloud-resolving simulations. *Journal of the Atmospheric Sciences*, 69(8), 2551–2565. <https://doi.org/10.1175/JAS-D-11-0257.1>
- Nolan, D., Rappin, E., & Emanuel, K. (2007). Tropical cyclogenesis sensitivity to environmental parameters in radiative-convective equilibrium. *Quarterly Journal of the Royal Meteorological Society*, 133(629 B), 2085–2107. <https://doi.org/10.1002/qj.170>
- Pope, K. N., Holloway, C. E., Jones, T. R., & Stein, T. H. M. (2021). Cloud-radiation interactions and their contributions to convective self-aggregation. *Journal of Advances in Modeling Earth Systems*, 13(9), e2021MS002535. <https://doi.org/10.1029/2021MS002535>
- Raymond, D. J., & Fuchs, Z. (2009). Moisture modes and the Madden-Julian oscillation. *Journal of Climate*, 22(11), 3031–3046. <https://doi.org/10.1175/2008JCLI2739.1>

- Ruckstuhl, C., Philipona, R., Morland, J., & Ohmura, A. (2007). Observed relationship between surface specific humidity, integrated water vapor, and longwave downward radiation at different altitudes. *Journal of Geophysical Research*, 112(D3), D03302. <https://doi.org/10.1029/2006JD007850>
- Sherwood, S. C., Webb, M. J., Annan, J. D., Armour, K. C., Forster, P. M., Hargreaves, J. C., et al. (2020). An assessment of Earth's climate sensitivity using multiple lines of evidence. *Reviews of Geophysics*, 58(4), e2019RG000678. <https://doi.org/10.1029/2019RG000678>
- Tobin, I., Bony, S., Holloway, C. E., Grandpeix, J.-Y., Sèze, G., Coppin, D., et al. (2013). Does convective aggregation need to be represented in cumulus parameterizations? *Journal of Advances in Modeling Earth Systems*, 5(4), 692–703. <https://doi.org/10.1002/jame.20047>
- Vaquero-Martínez, J., Antón, M., Ortiz de Galisteo, J. P., Román, R., & Cachorro, V. E. (2018). Water vapor radiative effects on short-wave radiation in Spain. *Atmospheric Research*, 205, 18–25. <https://doi.org/10.1016/j.atmosres.2018.02.001>
- Wing, A. A., & Cronin, T. W. (2016). Self-aggregation of convection in long channel geometry. *Quarterly Journal of the Royal Meteorological Society*, 142(694), 1–15. <https://doi.org/10.1002/qj.2628>
- Wing, A. A., Emanuel, K., Holloway, C. E., & Muller, C. (2017). Convective self-aggregation in numerical simulations: A review. *Surveys in Geophysics*, 38(6), 1173–1197. <https://doi.org/10.1007/s10712-017-9408-4>
- Wing, A. A., & Emanuel, K. A. (2014). Physical mechanisms controlling self-aggregation of convection in idealized numerical modeling simulations. *Journal of Advances in Modeling Earth Systems*, 6(1), 59–74. <https://doi.org/10.1002/2013MS000269>
- Wing, A. A., Reed, K. A., Satoh, M., Stevens, B., Bony, S., & Ohno, T. (2018). Radiative-Convective Equilibrium Model Intercomparison Project. *Geoscientific Model Development*, 11(2), 793–813. <https://doi.org/10.5194/gmd-11-793-2018>
- Wing, A. A., Stauffer, C. L., Becker, T., Reed, K. A., Ahn, M.-s., Arnold, N., et al. (2020). Clouds and convective self-aggregation in a multi-model ensemble of radiative-convective equilibrium simulations. *Journal of Advances in Modeling Earth Systems*, 12(9), e2020MS0021380. <https://doi.org/10.1029/2020MS0021380>
- Yang, D. (2018a). Boundary layer diabatic processes, the virtual effect, and convective self-aggregation. *Journal of Advances in Modeling Earth Systems*, 10(9), 2163–2176. <https://doi.org/10.1029/2017ms001261>
- Yang, D. (2018b). Boundary layer height and buoyancy determine the horizontal scale of convective self-aggregation. *Journal of the Atmospheric Sciences*, 75(2), 469–478. <https://doi.org/10.1175/JAS-D-17-0150.1>